Eng. Sci., 2023, **22**, 855

Engineered Science
DOI: https://dx.doi.org/10.30919/es8d855

Machine-learning-based, Online Estimation of Ceramic's Microstructure Upon the Laser Spot Brightness during Laser Sintering

Jianan Tang,[1, 3,*] Siddhartha Sarkar,[2] Hua Huang,[2] Xiao Geng,[2] Jianhua Tong,[2] Lionel Vargas-Gonzalez,[4] Nicholas Ku,[4] Dongsheng Li,[5] Hai Xiao[1, 3,*] and Fei Peng[2, 3,*]

Abstract

The ceramic microstructure strongly influences its properties. During manufacturing, the online monitoring of microstructure is critical to ensure the desired material properties. So far, the microstructure on the relevant scale is usually characterized offline using scanning electron microscopy (SEM), which is time and cost-consuming. In this work, we demonstrate a cost-effective, machine learning (ML)-based approach to simulate the SEM micrographs in real-time from the laser spot brightness. We experimentally observed a strong correlation between the laser spot brightness and the corresponding microstructure at the exact locations. The brightness values obtained from thermal emission images and the corresponding SEM micrographs were used in the training datasets. The ML algorithm was a style-based conditional generative adversarial network (CGAN). After training, the ML model could generate high-fidelity microstructure images within 0.1 seconds based on *in-situ* captured brightness at the laser sintering spot. We used the average grain sizes as the metric to evaluate the accuracy of the ML-predicted micrographs. The ML-predicted microstructures were in good agreement, with less than a 5% in difference from the real SEM images. In conclusion, we demonstrate the cost-effective, online microstructure estimation during laser sintering with a simple setup (a camera, a regular computer, and the ML model).

Keywords: Ceramics**;** Laser sintering; Microstructure, Machine learning; In situ monitoring.
Received: 29 November 2022; Revised: 21 March 2023; Accepted: 23 March 2023.
Article type: Research article.

1. Introduction

The properties of a ceramic material are dramatically influenced by its microstructure. The microstructural features, such as grain size, grain boundaries, pores, and defects, have strong correlations with the mechanical, thermal, and electrical properties of the ceramics, such as yielding strength, hardness, thermal conductivity, electrical conductivity, *etc*.[1] Scanning electron microscopy (SEM) is often used to characterize the microstructural features at the needed scale. This characterization must be carried out after the material is processed. So far, *in situ,* monitoring of ceramic microstructure during processing has yet to be achieved.

Recently, it has been demonstrated that the ultra-fast reactive laser sintering of ceramics that achieves the desired microstructure and crystalline phase within ~10 seconds].[2-9] It was found that the microstructure was sensitive to processing conditions such as laser power. Thus, a real-time, online monitoring method of the microstructure during laser sintering is urgently needed.

The current online monitoring and control during manufacturing are primarily focused on the precision of processing parameters themselves and of the dimensional control.[10,11] Specifically for ceramic sintering, the central

---

[1] *Department of Electrical and Computer Engineering, Clemson University, Clemson, SC 29634, USA.*
[2] *Department of Materials Science and Engineering, Clemson University, Clemson, SC, 29634, USA.*
[3] *Center for Optical Materials Science and Engineering Technologies (COMSET), Clemson University, Anderson, SC 29625, USA.*
[4] *DEVCOM Army Research Laboratory, Aberdeen Proving Ground, Aberdeen, MD 21005.*
[5] *Advanced Manufacturing LLC, East Hartford, CT 06108, USA.*
**Email:* fpeng@clemson.edu (F. Peng), haix@clemson.edu (H. Xiao), jianant@clemson.edu (J. Tang)

processing parameters are the sintering temperature and time. The temperature can be measured using either a thermocouple or a pyrometer. For example, during laser-based additive manufacturing of metals, pyrometers are often used to measure the melt pool temperature.[12,13] However, this method is not remarkably accurate for laser sintering ceramics. During the laser sintering of ceramics, there is no melt pool, and the surface emissivity constantly changes during consolidation and phase transformation. Thus, in this paper, we directly correlate the laser spot brightness with the resulting microstructure using the data model without seeking accurate temperature measurements at the laser spot.

ML methods such as Generative Adversarial Networks (GAN)[14] have shown great success in image generation, including microstructural images of materials.[15,16] A GAN consists of a generator and a discriminator, both of which are often constructed with deep neural networks. The generator is trained to generate high-fidelity samples like training data, while the discriminator is trained to distinguish the generated samples from the real ones. By training the generator and the discriminator iteratively, they can converge to a Nash equilibrium, where the generator is able to generate genuine samples and the discriminator cannot distinguish them from the real ones.[14] The generated microstructure images have high fidelity in microstructural features and resulting properties. A GAN was applied to generate oolitic Ketton limestone micro-computed tomography (micro-CT) images.[17] Material properties such as effective permeability were successfully obtained from the generated images. The same methodology was further adapted to generate multi-phase electrode microstructures.[18] The GAN-generated images were in good agreement with the real ones regarding microstructural features and relative diffusivity. In addition, GAN can generate images very quickly due to the utilization of convolutional layers.[19] The number of float point operations involved in microstructure generation is about a few billion, which can be processed by modern CPUs and GPUs in less than one second.

An important variant of GAN, conditional GAN (CGAN), incorporates additional information, known as conditions, into image generation and controls the features in the generated image.[20,21] Recently, researchers started to use CGANs to generate microstructure images according to different processing parameters.[22] For example, a CGAN with an auxiliary classifier was trained on the ultra-high carbon steel database, where many microstructural images were labeled with different cooling methods.[23] The trained CGAN was then used to synthesize high-quality multiphase microstructures given a cooling method. Another CGAN was trained to understand the sophisticated effect of the concentrations of Al and O on the microstructures when depositing Cr-Al-O-N thin film.[24] High-fidelity microstructure images could be predicted for new compositions.

In our previous study, a modified CGAN that can accurately predict microstructure evolution under various processing conditions[25] was demonstrated. For example, highly realistic SEM micrographs of laser-sintered alumina were simulated under various laser powers. The GAN-predicted microstructure evolution during the second phase growth fit the Johnson–Mehl–Avrami (JMA) equation well. In this paper, an improved algorithm is studied to predict the microstructures of laser-sintered ceramic $BaCe_{0.7}Zr_{0.1}Y_{0.1}Yb_{0.1}O_3$ (BCZYYb) from the thermal emission brightness. Fig. 1 illustrates the overview of this work. A camera was used to monitor the thermal emissions when the laser beam heated and sintered the ceramic sample. A modified CGAN took the brightness of the thermal emission as an indicator to generate the microstructure images in real-time. The generated microstructure images agreed with the real ones both visually and quantitatively.

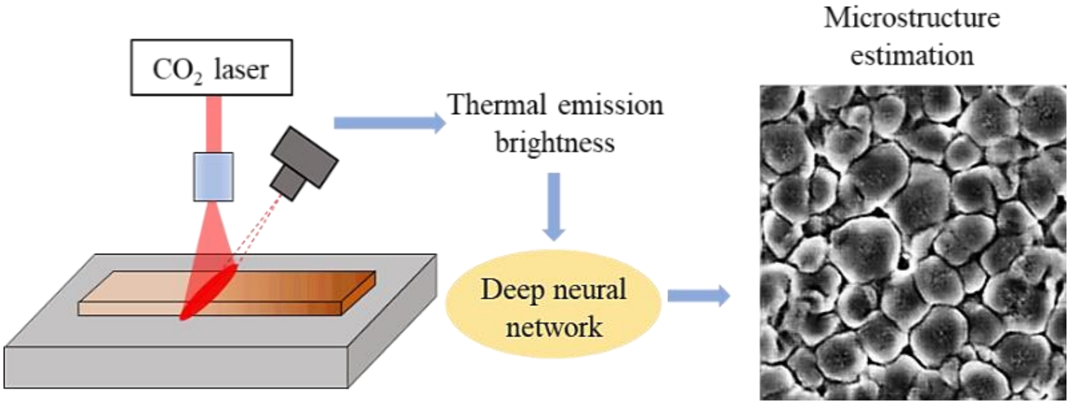

Fig. 1 Overview of the approach of using a deep neural network to generate microstructure images in real-time based on thermal emission brightness during laser sintering.

2. Experimental Methods

2.1 Laser sintering system with *in-situ* monitoring

Figure 2 shows the schematic of the laser sintering system with an *in-situ* monitoring camera. A carbon dioxide laser with a wavelength of 10.6 µm (Synrad P100, SYNRAD, Inc.) was used as the energy source for sintering. The laser beam was focused into a line-shaped beam by a cylindrical ZnSe lens. The focus distance of the lens was 25.4 mm. The laser was defocused 30 mm from the sample surface to enlarge the laser spot. On the sample surface, the laser spot was an ellipse with an 18 mm length and a 4 mm width. The power of the laser was set at 46 W. A translation stage carried the sample to scan through the laser beam. The scanning speed was kept at 0.1 mm/s.

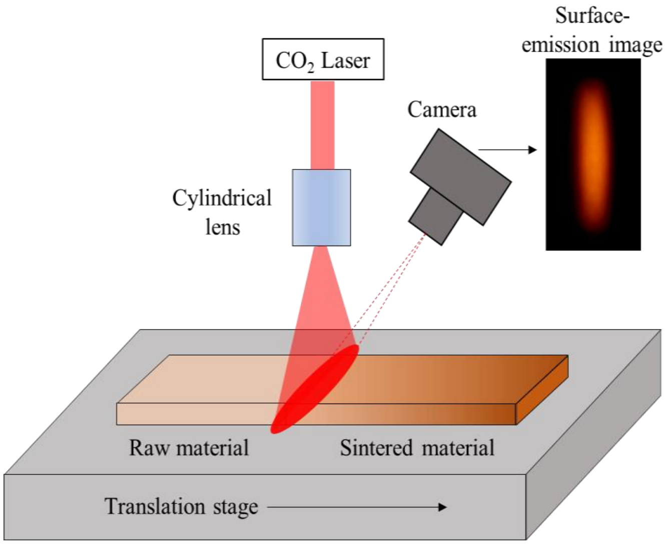

Fig. 2 Schematic of the laser-based additive manufacturing system with in-situ monitoring camera. The surface-emission image at the laser sintering spot is captured by the camera.

Surface emission images were captured using a camera (Canon EOS 90D) during the laser sintering process. The camera aimed at the laser spot at about 50° relative to the vertical axis. The relative position between the camera and the laser spot was fixed. In the camera's field of view, the laser spot did not move. The shutter of the camera was synchronized with the translation stage. Thus, the timestamp of a surface-emission image could be accurately translated to the position of the sintering spot. The shooting parameters of the camera, such as ISO sensitivity, shutter speed, and aperture size, are listed in Table 1. Since the complementary metal-oxide semiconductor (CMOS) sensor was only sensitive to 400 – 700 nm wavelength of light.[26] The laser spot images did not contain any surface reflection from the laser (wavelength = 10.6 µm).

2.2 Thermal emission brightness sampling

In a surface-emission image captured by the camera, the brightness distribution was a two-dimensional Gaussian-like distribution, as shown in Fig. 3. The raw image was a color image with three color channels (red, green, and blue). The image from the red channel was chosen, and the other two channels were discarded because the red channel had a high sensitivity to thermal emission.

A 5 × 5-pixel square at the peak was sampled to calculate the peak brightness as a representative feature of the surface-emission image. The actual area of the square in the sample was 500 × 500 µm^2. Thermal emission brightness was calculated from the average pixel value over the sampling area.

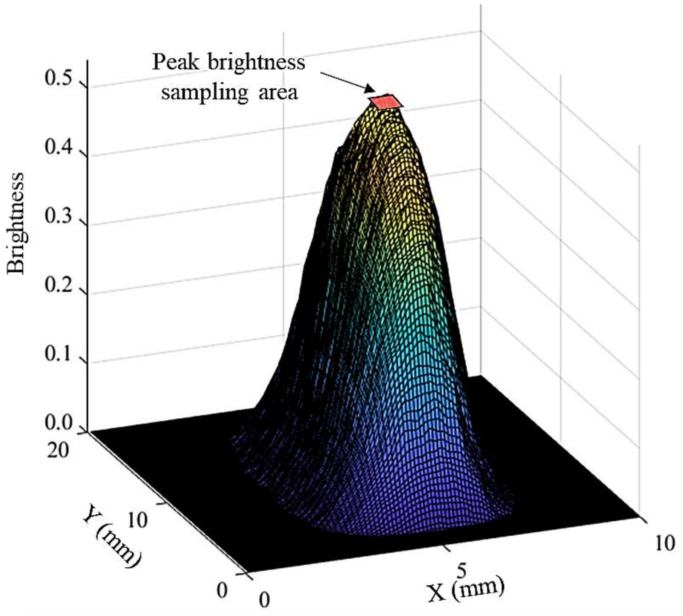

Fig. 3 Surface-emission image's brightness distribution. A small sampling area (500 × 500 µm^2) at the peak is selected to calculate thermal emission brightness. This area of the sample was then characterized using SEM.

2.3 Material preparation

The material system (BCZYYb) is a proton-conducting ceramic that has high protonic conductivity at relatively low temperatures (250~600 °C).[6] It has been used to fabricate

Table 1. Camera shooting parameters.

ISO sensitivity	Shutter speed	Aperture size	Image size	Shooting speed	Light wavelength range
100	1/12500 second	1/25	1080 × 1920 pixels	30 fps	400 – 700 nm

high-performance ceramic fuel cells,[27] electrolysis cells,[28] and membrane reactors.[29] The prepared sample was a half-cell of a protonic fuel cell, which consisted of two layers. The bottom layer was $BaCe_{0.7}Zr_{0.1}Y_{0.1}Yb_{0.1}O_3$ (BCZYYb) with 40 wt.% NiO addition as the anode. The top layer was BCZYYb with 1 wt.% NiO as the electrolyte.

The powder pastes of the BCZYYb NiO additive were prepared using ball-milling of the raw materials powders of $BaCO_3$ (99.8%, Alfa Aesar, Ward Hill, MA) Fe_2O_3 (99.9%, Alfa Aesar, Ward Hill, MA), CeO_2 (99.9%, Alfa Aesar, Ward Hill, MA), ZrO_2 (99.7%, Alfa Aesar, Ward Hill, MA), NiO (Ni 78.5%, Alfa Aesar, Ward Hill, MA), Y_2O_3 (99.9%, Alfa Aesar, Ward Hill, MA), and Yb_2O_3 (99.9%, Alfa Aesar, Ward Hill, MA)] for 48 h in the stoichiometric ratio, followed by mixing of the ball-milled powder with water, dispersant (Darvan 821A), and binder ((hydroxypropyl) methyl cellulose (HPMC)), as reported in.[30]

A green anode ceramic film was processed using direct ink writing on a fused silica substrate. The thin film with a uniform thickness of about 500 μm was deposited and dried in the ambient atmosphere for 24 h. The thin electrolyte layer was deposited on the printed anode film by spray coater. The thickness of the electrolyte layer was about 20 μm. The detailed anode layer processing and spray coating processing were described in our previous paper.[30]

2.4 SEM image acquisition and Preprocessing

After the sample was sintered using the CO_2 laser, the surface microstructures were characterized using a scanning electron microscope (SEM Hitachi S4800). Eight sampling spots on the surface were selected. Each sampling spot was a 500 × 500 μm^2 square. At each sampling spot, five non-overlapping SEM micrographs with 1,000× magnification were taken.

The collected SEM micrographs were grayscale images and 896 × 1280 pixels in size. One example is shown in Fig. 4. The full-size images were segmented into smaller

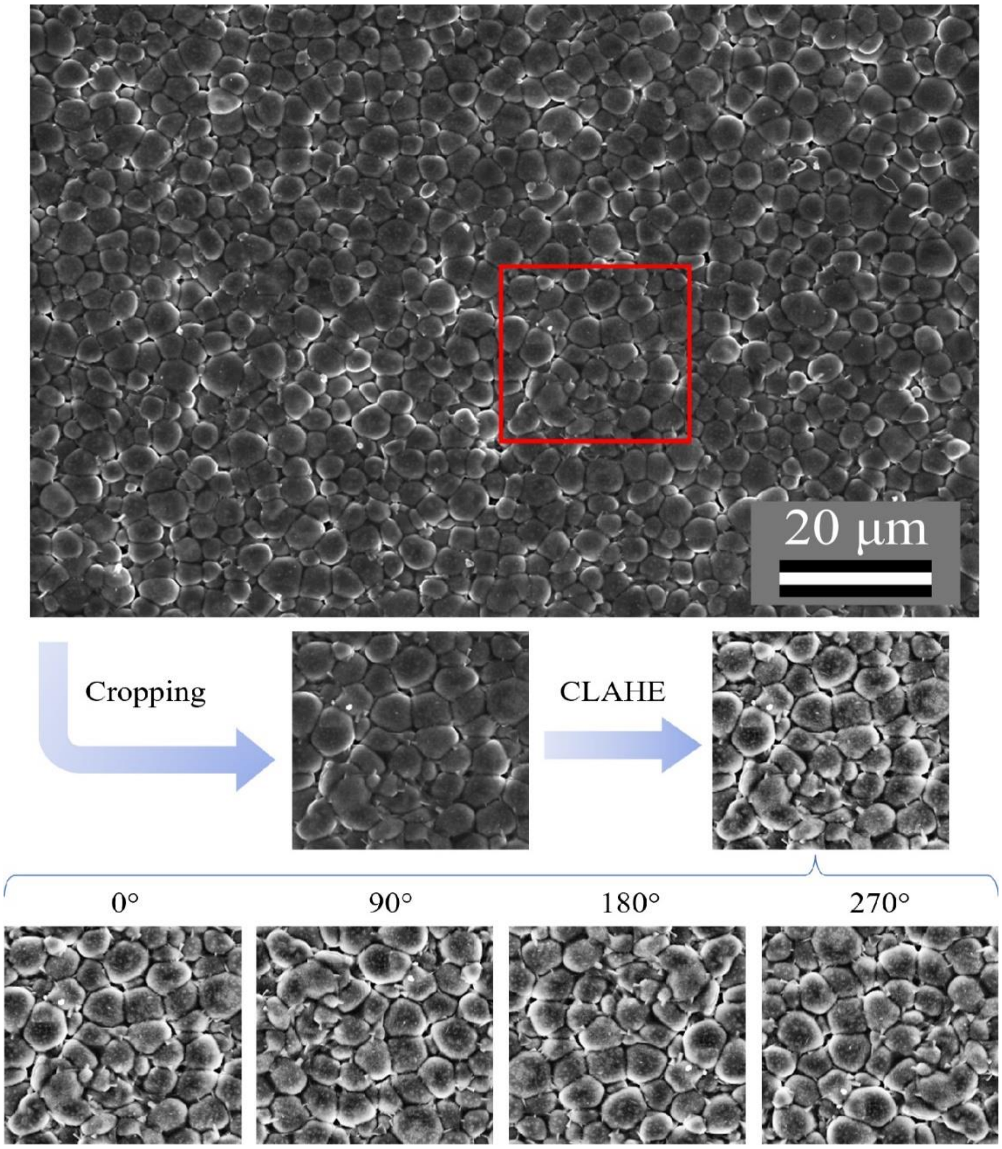

Fig. 4 Data preprocessing steps: cropping, contrast enhancement, and rotation.

micrographs because the original image size was too large. The size of the segmented images was 256 × 256 pixels, corresponding to 25.6 × 25.6 μm^2 in the sample. Two adjacent segments overlapped with each other by half. After segmentation, one full-size SEM micrograph was converted to 54 small micrographs. To normalize the contrast of the images, contrast-limited adaptive histogram equalization (CLAHE)[31] was applied. The window size of CLAHE was 8 × 8. And the contrast limit was 1.0. After CLAHE, the grain boundaries were more visible compared with the original image, as shown in Fig. 4. In addition, it was noticed that the grains in the micrographs were isotropic, which meant they were rotationally equivalent. Every micrograph was rotated by 90, 180, and 270 degrees to quadruple the size of the dataset. Due to the rotational equivalency of the grains, this data augmentation technique did not distort the original microstructure features. It is also widely believed that augmenting images by rotation can prevent deep learning algorithms from overfitting.[32]

2.5 Conditional Generative Adversarial Network

The Conditional Generative Adversarial Network consists of a generator G and a discriminator D, as shown in Fig. 5(a). The generator takes brightness y and a random seed z to generate a micrograph $\tilde{x}$. The discriminator takes a real micrograph x, or a generated micrograph $\tilde{x}$ along with the condition y and outputs a validity score. The validity score represents the confidence of the discriminator about whether the input image is real. The discriminator is trained to maximize the validity score by backpropagation.[33] At the same time, the generator is trained to minimize the validity score by improving the fidelity of the generated image. Once training is achieved, the generator will be able to fool the discriminator by generating genuine images just like the real ones. Mathematically, the discriminator and the generator play a minimax game described by the loss function[20,34]

$$\min_G \max_D E_{x|y\sim P_r}[D(x|y)] - E_{z\sim P_z}[D(G(z|y)|y)] \quad (1)$$

where P_r is the distribution of the real data and P_z is the distribution where the random seed is drawn.

The structure of the conditional generator is shown in Fig. 5(b). A random seed and the brightness value are fed through two fully connected layers, respectively, and then concatenated together to form an 8 × 8 × 116 feature map. The feature map is then scaled up by a transposed convolutional layer with a 5 × 5 kernel size and a stride of 2 to 16 × 16 × 64. The upscaled feature map is then passed through a residual block,[35] so the receptive field of each pixel is enlarged, and the depth of the network is increased. The feature map continues to pass through another 4 stacks of convolutional layers and residual blocks. The final layer is a convolutional layer with an 11 × 11 kernel size and a stride of 1. The activation functions used by dense layers, convolutional layers, and transposed convolutional layers are LeakyReLU,[36] except for the final layer. The final layer uses a hyperbolic tangent function as its activation function to cast the output pixel value between -1 and 1.

To compare the performance of the conditional generator, we investigated a style-based generator[21] as shown in Fig. 5(c). A random seed is fed to a fully connected layer to obtain the initial feature map with a size of 8 × 8 × 64. The condition (brightness value) is processed by another fully connected layer to obtain a styled vector. The feature map is upscaled by a transposed convolutional layer with a 5 × 5 kernel size and a stride of 2. Then the style vector is applied to the feature map by an adaptive instance normalization layer[37] and adjusts the mean and standard deviation of the feature map. The result then passes through a residual block. Another 4 stacks of one transposed convolutional layer, one adaptive instance normalization layer, and one residual block follow behind. convolutional layer with 11 × 11 kernel size and a stride of 1. The activation functions used by dense layers, convolutional layers, and transposed convolutional layers are LeakyReLU,[31] except for the final layer. The final layer uses a hyperbolic tangent function as its activation function to cast the output pixel value between -1 and 1.

The discriminator's structure is inspired by ResNet,[35] as shown in Fig. 5(d). The input 256 × 256 images are first down-sampled by a convolutional layer with 5 × 5 kernel size and a stride of 2 and further down-sampled by a max-pooling layer with 2 × 2 kernel size. The resulting feature map is concatenated to a condition vector obtained by passing the brightness value through a fully connected layer. Then the result passes through 4 stacks of one transposed convolutional layer and one residual block. The feature map is down-sampled to 4 × 4 × 320. A fully connected layer with 320 neurons and a fully connected layer with 1 neuron converts the feature map to a single scalar output.

The network was implemented using Keras,[38] and the implementation details can be found at https://github.com/tojunesa/RCWGAN-GP/blob/main/RCWGAN-GP.ipynb. To stabilize the training, Wasserstein distance[39] was used as the loss function, and a gradient penalty[40] was employed for regularization. The weight coefficient of gradient penalty loss was set to 1. The network was trained using mini-batch gradient descent, and the adaptive moment estimation algorithm (Adam)[41] was utilized as the optimizer. The initial learning rate was set to 1e-

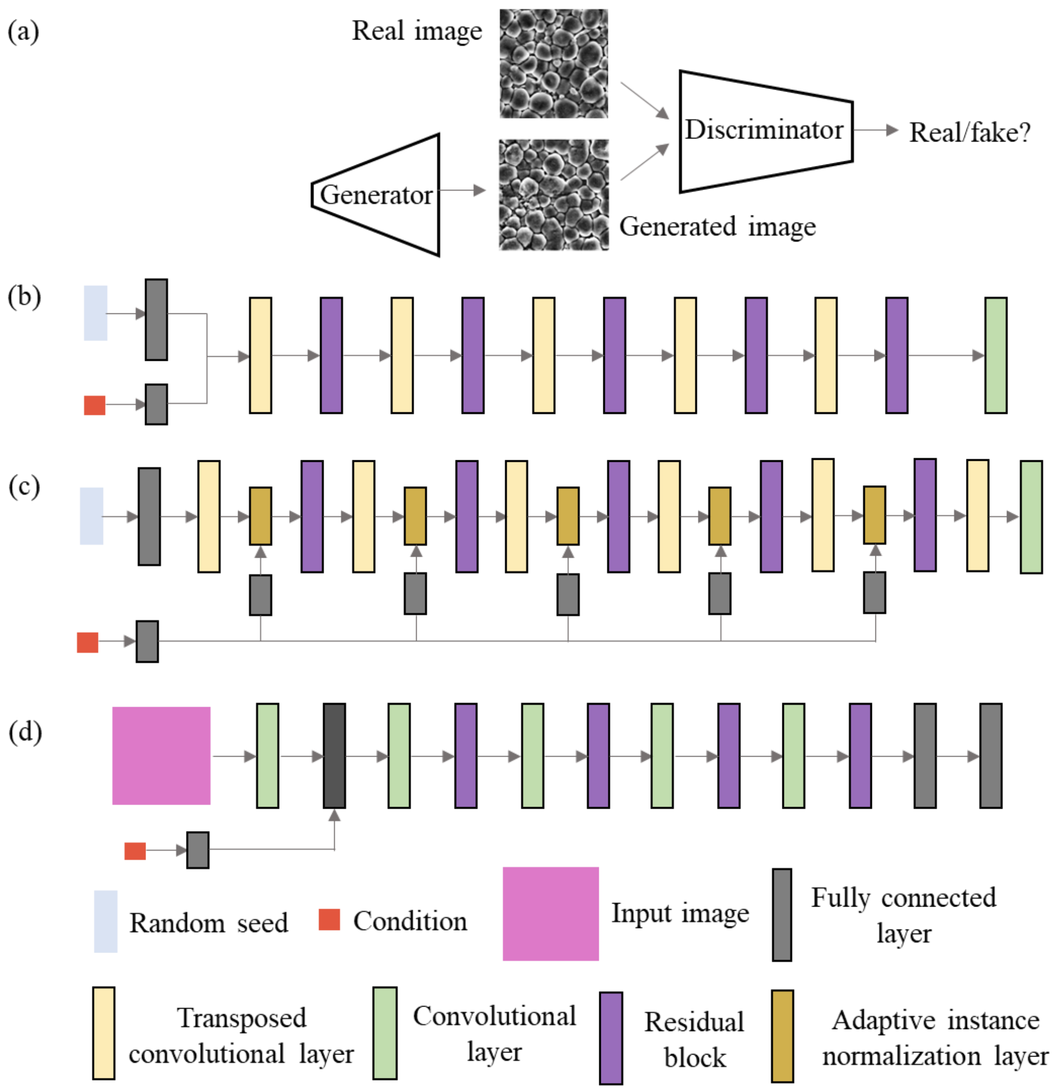

Fig. 5 Network structure. (a) CGAN's structure. (b) Conditional generator's structure. (c) Style-based generator's structure. (d) Conditional discriminator's structure.

5 for the generator and 2e-5 for the discriminator, which is inspired by the two-time scale update rule proposed by Heusel *et al.*.[42] The network was trained for 50 epochs on Palmetto, the high-performance computing cluster of Clemson University. It took 4 hours to complete the training on 40 CPUs and 2 GPUs (Nvidia V100).

2.6 Average grain size characterization

The average grain sizes for real SEM and GAN-generated SEM were measured from a micrograph using the standard ASTM E112 - 10 method.[43] This standard is suitable for the grain size characterization for randomly oriented, equiaxed grains. The average grain size was calculated based on the number of grains per unit area for a specific SEM magnification. Specifically, one individual micrograph in a training set had a size of 256 × 256 pixels. As one pixel corresponds to 0.1 μm, the area of the micrograph can be interpreted as 25.6 × 25.6 μm^2. Then the average grain size was calculated based on ASTM E112 - 10.

The equation for calculating the average grain size is given as follows:

$$d = \frac{10^9}{M^2} \times \sqrt{\frac{1}{\ln(N_{grain} \times a)}} \tag{2}$$

where d is the average grain size in micrometers, M is the magnification (*i.e.*, 1000× for this study) N_{grain} is the number of grains per 25.6 × 25.6 mm^{2}in the micrograph, a is an empirical constant equal to 6097.

3. Results and discussions

3.1 Laser spot brightness and corresponding microstructure

A strong correlation between laser spot brightness and the corresponding microstructure was observed. As shown in Fig. 6, thermal emission brightness fluctuated during laser

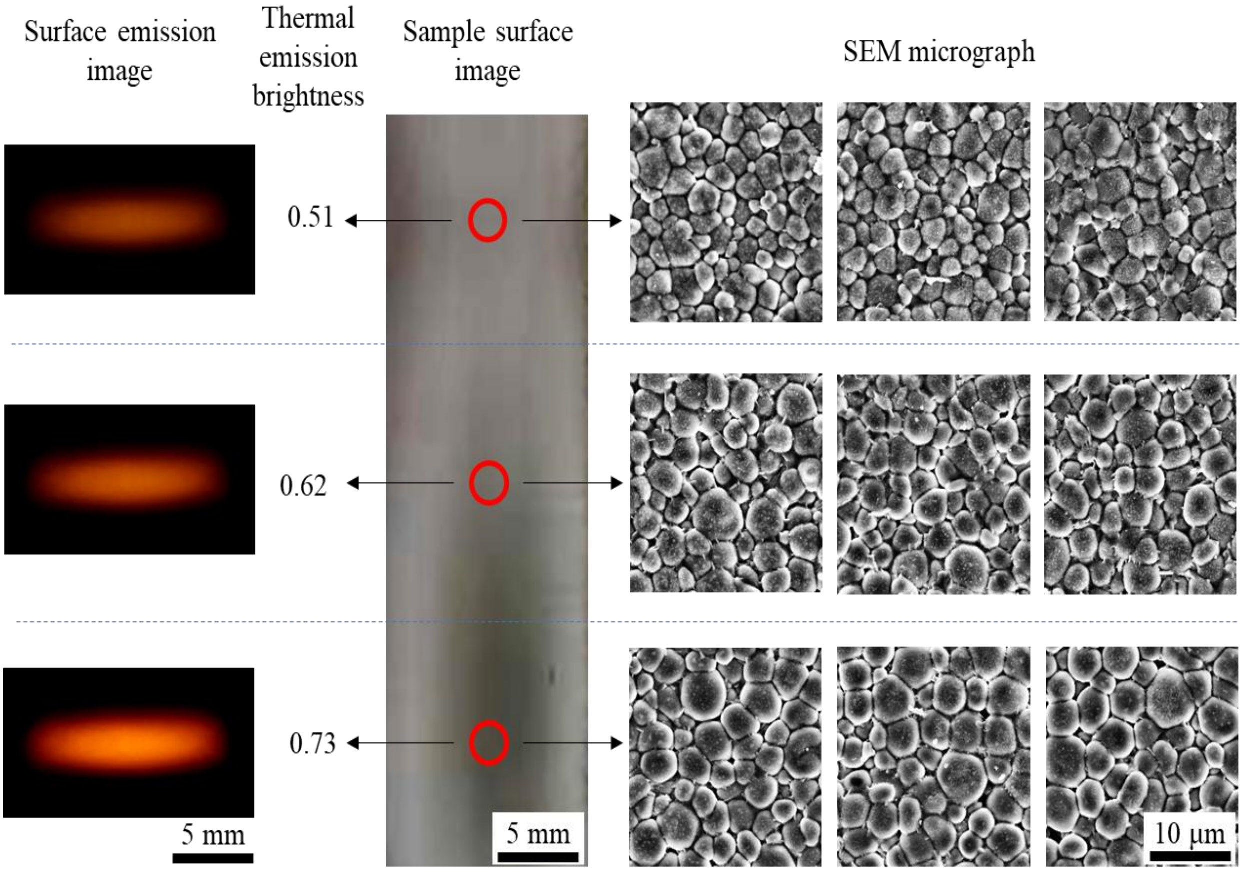

Fig. 6 A strong correlation between laser spot brightness and microstructure was observed. The surface-emission images, peak brightness values, sample surface picture, and corresponding SEM micrographs at three different locations (marked by red circles) show the microstructure changes as the peak brightness changes.

sintering. A dim spot corresponds to a fine microstructure with small average grain sizes. A bright spot resulted in a relatively coarse microstructure and larger grain sizes. Although it was difficult to accurately measure the surface temperature during laser sintering, the laser spot brightness was generally correlated with temperature. According to the sintering theories, a higher temperature usually results in larger grain sizes.

The physical cause behind the variation of thermal emission brightness could be manyfold.[44] Temperature variation due to unsteady laser output could be one of the causes. High-power carbon dioxide lasers are inevitably unstable due to passive Q-switch pulsation.[45] and thermal instability. Inconsistent heat dissipation through the baseplate could be another reason.[46] The variation of surface emissivity during laser sintering can also contribute to the brightness change.

3.2 Comparison of the performance of different generator structures

Two kinds of generator structures are described in section 2.5. The conditional generator directly concatenates the conditional information with the random seed at the very beginning.[20] While low-level features, such as grains' texture, are directly generated from the conditional information, high-level features, such as grain size, are calculated from the low-level features. The correlation between conditional information and high-level features could be difficult to learn. On the other hand, the style-based generator calculates style vectors for different resolution levels and uses them to adaptively adjust the statistical characteristics of feature maps. Thus, the style-based generator can disentangle the generation of low-level features, from the generation of high-level features, which could lead to better performance.[21,47] The results are shown in Fig. 7. For both the conditional and style-based generators, the generated micrographs were improved and closer to the ground truth as the number of training epochs increased. However, the conditional generator failed to capture the correlation between the brightness value and the microstructure features (*e.g.,* grain size). It produced the same micrograph disregarding the input conditions. The style-based generator outperformed the conditional generator. As the number of epochs increased, the style-based generator quickly grasped the knowledge that an increased brightness value

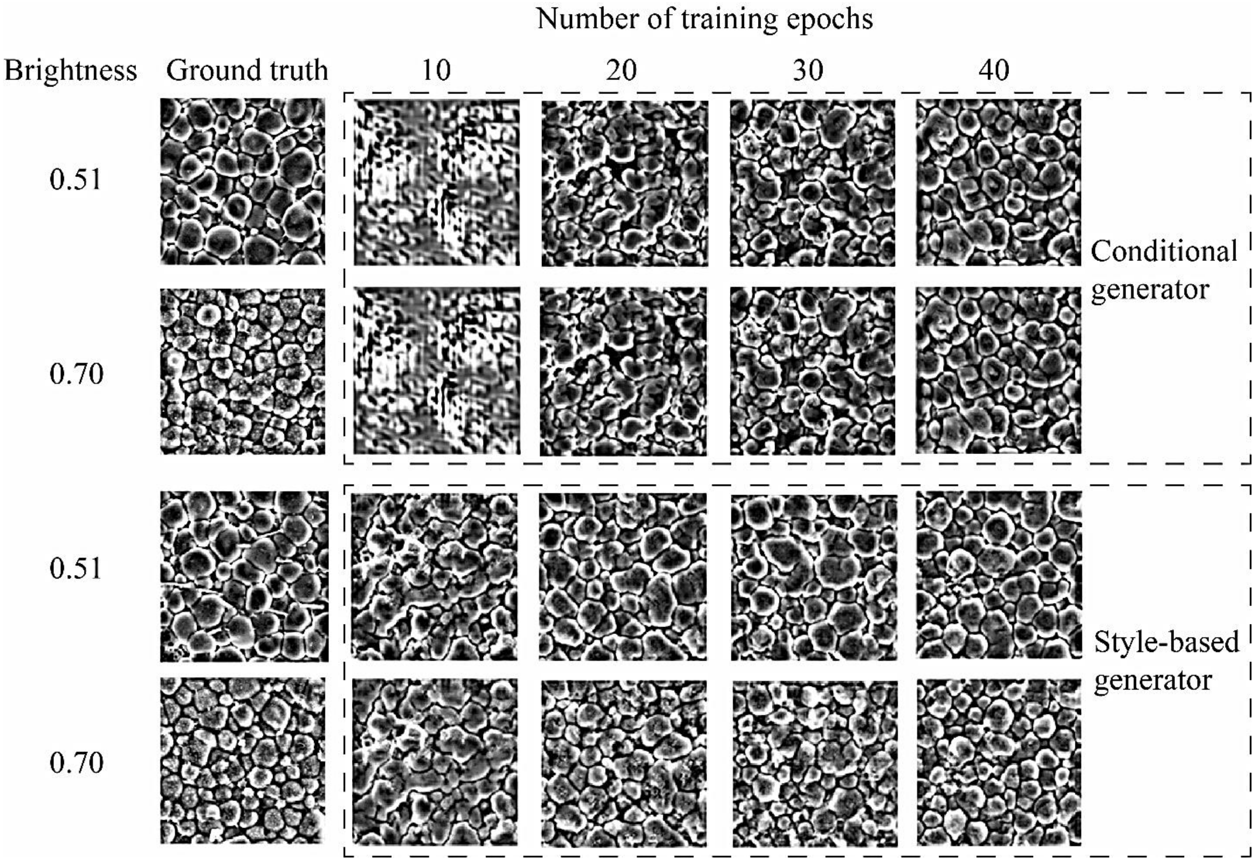

Fig. 7 The performance difference between conditional generator and style-based generator.

would lead to an increase in grain size. Thus, the style-based generator was selected for further studies.

3.3 Estimating the microstructure using the style-based CGAN from the laser spot brightness

The style-based CGAN took different thermal emission brightness values as the conditions to generate microstructure images. Several exemplar results are shown in Fig. 8 along with the real micrographs as the ground truth. By comparing the generated micrograph with the real micrograph corresponding to the same brightness value, the microstructure features, such as grain size and grain shape, are highly similar to the real SEM micrographs. The grains and grain boundaries are as clear as the actual micrographs.

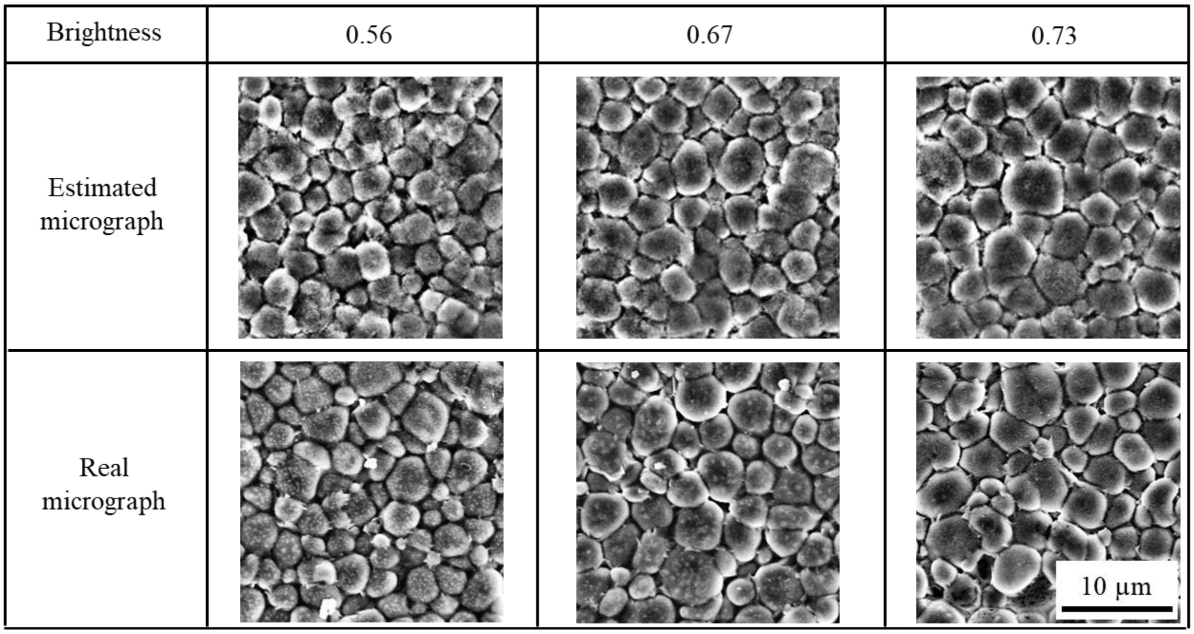

Fig. 8 Estimated micrographs and the real ones correspond to three exemplar peak brightness values.

The generated micrographs also accurately show the microstructure trend for the various laser spot brightness. From left to right, the grains grow larger as the brightness increases. Thus, the style-based CGAN's capability to generate high-fidelity microstructure images is demonstrated. The prediction performance of the style-based CGAN upon an arbitrary brightness was also tested. The brightness of 0.62 and its corresponding microstructures were left out as the test data, which means that the algorithm had never seen them. Fig. 9 compares the estimated micrographs when the style-based CGAN was conditioned with the 0.62 brightness and the real micrographs, experimentally obtained at the brightness of 0.62. The estimated micrographs show a high similarity to the real ones. It is concluded that the style-based CGAN does not generate high-fidelity micrographs by memorizing training examples but by capturing the correlation between the brightness and the microstructures.

The estimated micrographs were generated by feeding different random seeds into the CGAN. The geometric distribution of the grains varies among those micrographs, while features such as grain size and shape are kept the same. These randomly generated micrographs imitated the actual SEM micrographs because, typically, the microstructures are random but contain well-defined features. It indicates that the CGAN understands that the microstructure features are random distributions rather than deterministic constants, which agrees with the stochastic nature of the microstructures.

3.4 Quantitative evaluation

The style CGAN can generate SEM micrographs that are highly similar to the real SEM. A criterium is still needed to quantitatively measure the fidelity of the generated micrographs. The average grain size was selected as the criterium. This is because all the samples were almost fully dense after laser sintering. The grain size was the prominent microstructure feature that varied, corresponding to various spot brightness. The average grain sizes were measured in both real micrographs and CGAN-estimated ones. For each brightness value, ten real micrographs were randomly sampled. These real micrographs are sampled from the dataset after segmentation and contrast enhancement but before rotation. So, no micrograph was a duplicate of another one. Then ten estimated micrographs were generated using the CGAN. In each micrograph, the average grain size was measured by the method described in Section 2.6. The results are plotted in Fig. 10. The blue squares represent the mean value of the average grain sizes of the real micrographs. The red dots denote the mean value from the generated micrographs. The error bars mark the standard deviations in each subgroup.

The absolute differences in average grain size between the real micrographs and the generated ones are all below 0.09 μm. The mean absolute error (MAE) among all peak brightness values is 0.05 μm. On the train set, the MAE is 0.04 the μm. On the validation set, the MAE is 0.08 μm. Although the error on the validation set is larger than the average, compared with the average grain size change among the dataset (0.75 μm), the error is relatively small. In conclusion, the CGAN can generate different micrographs according to various brightness values accurately.

It is also noticed that the standard deviations in the generated micrographs tend to be larger. This is because some grain boundaries are blurred in the generated micrographs. When calculating the average grain size by hand, there were always human errors. This will be solved by gathering more

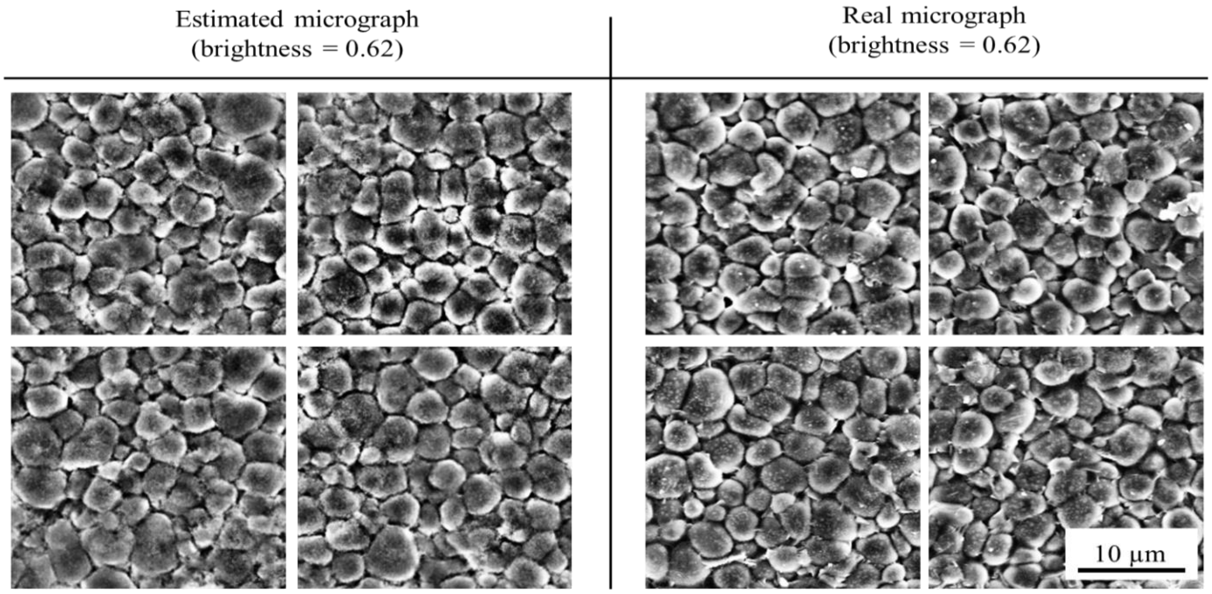

Fig. 9 The estimated micrographs and the real ones correspond to the brightness of 0.62, which is left out as validation data.

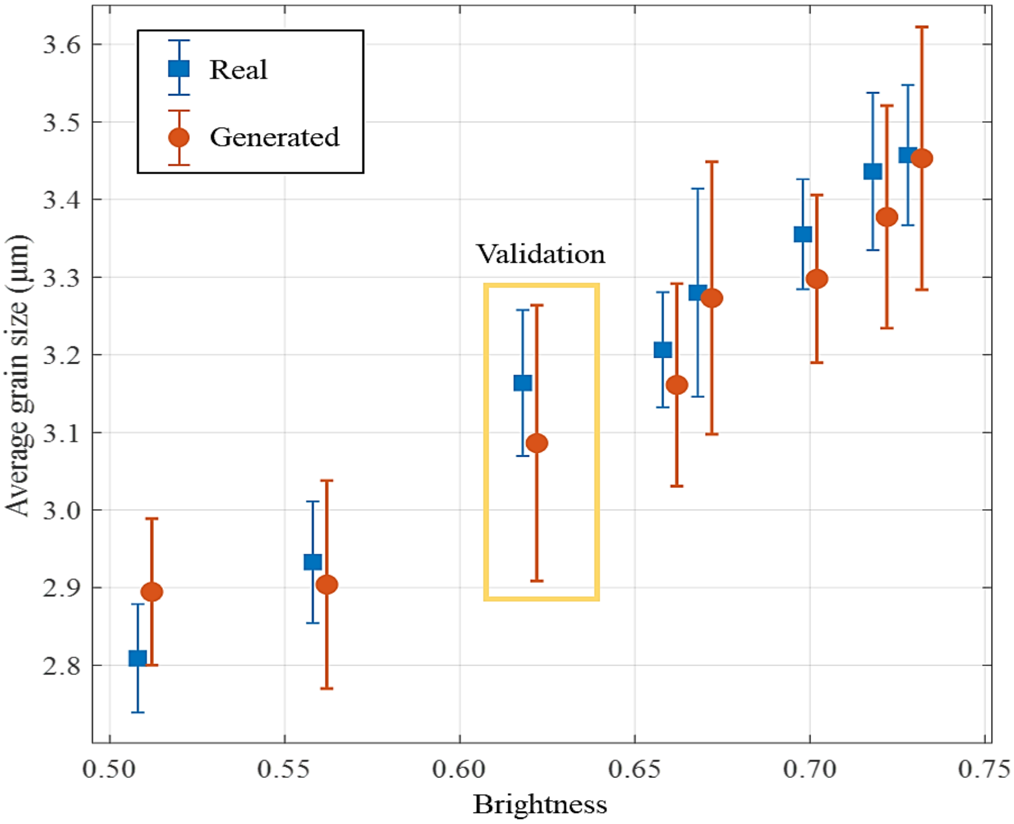

Fig. 10 Measured average grain sizes from the real micrographs and the generated ones.

experimental data and improving the algorithm in future work.

3.5 Real-time microstructure monitoring

To enable real-time microstructure monitoring, the machine learning model needs to generate the estimated micrographs quickly. Substantial progress has been made in the physics-based models that predict microstructures under known governing laws.[48-54] These methods include density function theory (DFT), phase field, Monte Carlo, *etc*. However, these physics-based models usually require high computational costs. It is unrealistic to use physics-based models for real-time microstructure prediction in advanced manufacturing systems. The data-driven machine learning (ML) approaches offer potent alternative tools to simulate the material's microstructure. After training, the data-driven ML algorithms can generate the simulation results almost instantly without knowing the governing laws.

In this study, the time needed to generate a micrograph using the style-based CGAN was tested. After training, the machine learning model typically can generate 10 micrographs in 1 second from the brightness value, which means it takes about 0.1 sec to generate one micrograph. The test was conducted using a regular personal computer with Intel(R) Core(TM) i7-6920HQ CPU @ 2.90GHz, and 32 G RAM.

Thus, we demonstrate a cost-effective, real-time microstructure monitoring method. The only equipment needed is a camera, a regular computer, and a trained ML model.

4. Conclusion

In this work, a cost-effective, online microstructure estimation method based on a novel machine-learning algorithm, style-based CGAN, is demonstrated. A camera captured the *in-situ* thermal emission during the laser sintering process. A strong correlation was observed between the thermal emission brightness at the center of the laser spot and the corresponding ceramic microstructure at the exact location. In general, an increase in brightness leads to an increase in grain size. Thus, the center laser spot brightness can be used as an indicator of the microstructure. The style-based CGAN learned this correlation after training and could generate high-fidelity micrographs whose microstructural features were close to the real ones. The style-based CGAN could also estimate the microstructure corresponding to a brightness value, not in the train set by interpolation. To quantitatively evaluate the fidelity of the estimated micrographs, the mean absolute error in average grain size was used as the metric. On the train set, the mean absolute error is 0.04 µm. The absolute error on the validation set is 0.08 µm. These results suggest that the generated microstructure images agree well with the real ones. In addition, the algorithm can generate one image in less than 0.1 seconds on a personal computer (*e.g.*, Intel(R) Core(TM) i7-6920HQ CPU @ 2.90GHz 2.90 GHz, 32 G RAM). This makes the machine learning model suitable for online estimation of the microstructure during laser sintering.

Acknowledgment

The authors would like to thank the funding support from DOE/NETL (Grant No. DE-FE0031826), DOE/EERE (Grant No. DE-EE0008428), DOE/NETL (DE-FE0032231), US Army (Grant No. W911NF-23-2-0058), and NIH (Grant No. P20GM121342).

Conflict of Interest

There is no conflict of interest.

Supporting Information

Not applicable.

References

[1] W. E. Lee, M. Rainforth, Ceramic microstructures: property control by processing, Springer Science & Business Media, 1994.

[2] X. Geng, J. Tang, B. Sheridan, S. Sarkar, J. Tong, H. Xiao, D. Li, R. K. Bordia, F. Peng, Ultra-Fast laser fabrication of alumina micro-sample array and high-throughput characterization of microstructure and hardness, *Crystals*, 2021, **11**, 8, 890, doi: 10.3390/cryst11080890.

[3] X. Geng, Y. Hong, J. Lei, J. Ma, J. Chen, H. Xiao, J. Tong, R. K. Bordia, F. Peng, Ultra-fast, selective, non-melting, laser sintering of alumina with anisotropic and size-suppressed grains, *Journal of the American Ceramic Society*, 2021, **104**, 1997-2006, doi: 10.1111/jace.17617.

[4] S. Mu, Z. Zhao, H. Huang, J. Lei, F. Peng, H. Xiao, K. S. Brinkman, J. J. Tong, Advanced manufacturing of intermediate-temperature protonic ceramic electrochemical cells, *The Electrochemical Society Interface*, 2020, **29**, 67, doi: 10.1149/2.F09204IF.

[5] A. Ishii, S. Mu, Y. Meng, H. Huang, J. Lei, Y. Li, F. Peng, H. Xiao, J. Tong, K. S. Brinkman, Rapid Laser Processing of Thin Sr-Doped LaCrO3–δ Interconnects for Solid Oxide Fuel Cells, *Energy Technology*, 2020, **8**, 2000364, doi: 10.1002/ente.202000364.

[6] S. Mu, H. Huang, A. Ishii, Z. Zhao, M. Zou, P. Kuzbary, F. Peng, K. Brinkman, H. Xiao, J. Tong, Rapid laser reactive sintering of $BaCe_{0.7}Zr_{0.1}Y_{0.1}Yb_{0.1}O_{3-\delta}$ electrolyte for protonic ceramic fuel cells, *Advanced Materials Technologies*, 2020, **5**, 2000281, doi: 10.1002/admt.202000281.

[7] J. Lei, Q. Zhang, Z. Zhao, Y. Chen, J. Gao, J. Tong, F. Peng, H. Xiao, One-step fabrication of nanocrystalline nanonetwork SnO_2 gas sensors by integrated multilaser processing, *Advanced Materials Technologies*, 2020, **5**, 2000281, doi: 10.1002/admt.202000281.

[8] S. Mu, H. Huang, A. Ishii, Y. Hong, A. Santomauro, Z. Zhao, M. Zou, F. Peng, K. S. Brinkman, H. Xiao, J. Tong, Rapid laser reactive sintering for sustainable and clean preparation of protonic ceramics, *ACS Omega*, 2020, **5**, 11637-11642, doi: 10.1021/acsomega.0c00879.

[9] S. Mu, Y. Hong, H. Huang, A. Ishii, J. Lei, Y. Song, Y. Li, K. S. Brinkman, F. Peng, H. Xiao, J. Tong, A novel laser 3D printing method for the advanced manufacturing of protonic ceramics, *Membranes*, 2020, **10**, 98, doi: 10.3390/membranes10050098.

[10] U. Berger, J. Selka, A. Ampatzopoulos, J. Klabuhn, Manufacturing cyber-physical systems (industrial Internet of Things), *Industrial Internet of Things*, Cham: Springer International Publishing, 2016, 423-445, doi: 10.1007/978-3-319-42559-7_16.

[11] C. Kaestle, H. Fleischmann, M. Scholz, S. Haerter, J. Franke, Cyber-physical electronics production, *Industrial Internet of Things*, Cham: Springer International Publishing, 2016, 47-78, doi: 10.1007/978-3-319-42559-7_3.

[12] C.-G. Ren, Y. Lo, H. Tran, M. Lee, Emissivity calibration method for pyrometer measurement of melting pool temperature in selective laser melting of stainless steel 316L, *The International Journal of Advanced Manufacturing Technology*, 2019, **105**, 637 - 649, doi: 10.1007/s00170-019-04193-0.

[13] L. Song, V. Bagavath-Singh, B. Dutta, J. Mazumder, Control of melt pool temperature and deposition height during direct metal deposition process, *The International Journal of Advanced Manufacturing Technology*, 2012, **58**, 247-256, doi: 10.1007/S00170-011-3395-2.

[14] I. Goodfellow, J. Pouget-Abadie, M. Mirza, B. Xu, D. Warde-Farley, S. Ozair, A. Courville, Y. Bengio, Generative adversarial networks, *Communications of the ACM*, 2020, **63**, 139-144, doi: 10.1145/3422622.

[15] D. Fokina, E. Muravleva, G. Ovchinnikov, I. Oseledets, Microstructure synthesis using style-based generative adversarial network, *Physical Review E*, 2020, **101**, 043308, doi: 10.1103/PhysRevE.101.043308.

[16] J.-W. Lee, N. H. Goo, W. Park, M. Pyo, K. Sohn, Virtual microstructure design for steels using generative adversarial networks, *Engineering Reports*, 2021 **3**, e12274 10.1002/eng2.12274.

[17] L. Mosser, O. Dubrule, M. Blunt, Stochastic reconstruction of an oolitic limestone by generative adversarial networks, *Transport in Porous Media*, 2018, **125**, 81-103, doi: 10.1007/s11242-018-1039-9.

[18] A. Gayon-Lombardo, L. Mosser, N. Brandon, S. J. Cooper, Pores for thought: generative adversarial networks for stochastic reconstruction of 3D multi-phase electrode microstructures with periodic boundaries, *npj Computational Materials*, 2020, **6**, 1-11, doi: 10.1038/s41524-020-0340-7.

[19] K. O'Shea, R. Nash, An introduction to convolutional neural networks, 2015, arXiv: 1511.08458, https://arxiv.org/abs/1511.08458.

[20] M. Mirza, S. Osindero, Conditional generative adversarial nets, 2014: arXiv: 1411.1784, https://arxiv.org/abs/1411.1784.

[21] T. Karras, S. Laine, T. Aila, A style-based generator

architecture for generative adversarial networks, Proceedings of the IEEE/CVF conference on computer vision and pattern recognition, 2019, 4401-4410.

[22] W. Ma, E. J. Kautz, A. Baskaran, A. Chowdhury, V. Joshi, B. Yener, D. J. Lewis, Image-driven discriminative and generative machine learning algorithms for establishing microstructure–processing relationships, *Journal of Applied Physics*, 2020, **128**, 134901.

[23] A. Iyer, B. Dey, A. Dasgupta, W. Chen, A. Chakraborty, A conditional generative model for predicting material microstructures from processing methods, 2019: arXiv: 1910.02133, https://arxiv.org/abs/1910.02133.

[24] L. Banko, Y. Lysogorskiy, D. Grochla, D. Naujoks, R. Drautz, A. Ludwig, Predicting structure zone diagrams for thin film synthesis by generative machine learning, *Communications Materials*, 2020, **1**, 1-10, doi: 10.1038/s43246-020-0017-2.

[25] J. Tang, X. Geng, D. Li, Y. Shi, J.-H. Tong, H. Xiao, F. Peng, Machine learning-based microstructure prediction during laser sintering of alumina: a conditional generative approach, *Scientific Reports*, 2021, **11**, 1-10, doi: 10.1038/s41598-021-89816-x.

[26] J. L. Deglint, F. Kazemzadeh, D. S. Cho, D. A. Clausi, A. Wong, Numerical demultiplexing of color image sensor measurements via non-linear random forest modeling, *Scientific Reports*, 2016, **6**, 28665, doi: 10.1038/srep28665.

[27] C. Duan, D. Hook, Y. Chen, J. Tong, R. O'Hayre, Zr and Y co-doped perovskite as a stable, high-performance cathode for solid oxide fuel cells operating below 500 C, *Energy & Environmental Science*, 2017, **10**, 176-82, doi: 10.1039/C6EE01915C.

[28] C. Duan, R. Kee, H. Zhu, N. Sullivan, L. Zhu, L. Bian, D. Jennings, R. O'Hayre, Highly efficient reversible protonic ceramic electrochemical cells for power generation and fuel production, *Nature Energy*, 2019, **4**, 230-40, doi: 10.1038/s41560-019-0333-2.

[29] W. G. Coors, A. Manerbino, Characterization of composite cermet with 68 wt.% NiO and BaCe0.2Zr0.6Y0.2O3−δ, *Journal of Membrane Science*, 2011, **376**, 50-5, doi: 10.1016/j.memsci.2011.03.062.

[30] S. Mu, Z. Zhao, J. Lei, Y. Hong, T. Hong, D. Jiang, Y. Song, W. Jackson, K. Brinkman, F. Peng, H. Xiao, J. Tong, Engineering of microstructures of protonic ceramics by a novel rapid laser reactive sintering for ceramic energy conversion devices, *Solid State Ionics*, 2018, **320**, 369-377, doi: 10.1016/j.ssi.2018.03.023.

[31] K. Zuiderveld, Contrast limited adaptive histogram equalization, Graphics gems, 1994, 474-485.

[32] L. Perez, J. Wang, The effectiveness of data augmentation in image classification using deep learning, 2017, arXiv: 1712.04621, https://arxiv.org/abs/1712.04621.

[33] Y. LeCun, D. Touresky, G. Hinton, T. Sejnowski, A theoretical framework for back-propagation, Proceedings of the 1988 connectionist models summer school, 1988, 21-28.

[34] Antipov G, Baccouche M, Dugelay JL. Face aging with conditional generative adversarial networks, 2017 IEEE international conference on image processing, 2017, 2089-2093.

[35] K. He, X. Zhang, S. Ren, J. Sun, Deep residual learning for image recognition, Proceedings of the IEEE conference on computer vision and pattern recognition, 2016, 770-778.

[36] A. L. Maas, Rectifier nonlinearities improve neural network acoustic models, Proceedings of the 30th International Conference on Machine Learning, 2013.

[37] X. Huang, S. Belongie, Arbitrary style transfer in real-time with adaptive instance normalization. 2017 IEEE International Conference on Computer Vision (ICCV). October 22-29, 2017, Venice, Italy. IEEE, 2017, 1510-1519, doi: 10.1109/ICCV.2017.167.

[38] F. Chollet , others Keras [Internet]". GitHub; 2015. https://github.com/fchollet/keras.

[39] M. Arjovsky, S. Chintala, L. Bottou, Wasserstein generative adversarial networks, *International Conference on Machine Learning*, 2017, 214-223.

[40] I. Gulrajani, F. Ahmed, M. Arjovsky, V. Dumoulin, A. C. Courville, Improved training of wasserstein gans, *Advances in neural information processing systems*, 2017, 30.

[41] D. P. Kingma, J. Ba, Adam: A method for stochastic optimization, 2014: arXiv: 1412.6980. https://arxiv.org/abs/1412.6980.

[42] M. Heusel, H. Ramsauer, T. Unterthiner, B. Nessler, S. Hochreiter, GANs trained by a two time-scale update rule converge to a local Nash equilibrium, Advances in neural information processing systems, 2017, 30.

[43] ASTM E112-10: Standard Test Methods for Determining Average Grain Size, 2015.

[44] M. Grasso, B. Colosimo, Process defects and in situ monitoring methods in metal powder bed fusion: a review, *Measurement Science and Technology*, 2017, **28**, 044005, doi: 10.1088/1361-6501/aa5c4f.

[45] N. B. Abraham, L. A. Lugiato, L. M. Narducci, Overview of instabilities in laser systems, *JOSA B*, 1985, **2**, 7-14, doi: 10.1364/JOSAB.2.000007.

[46] K. Zeng, Optimization of support structures for selective laser melting, Doctoral Dissertation, 2015, Department of Industrial Engineering, University of Louisville, Louisville, Kentucky.

[47] Z. Wu, D. Lischinski, E. Shechtman, Stylespace analysis: Disentangled controls for stylegan image generation, Proceedings of the IEEE/CVF Conference on Computer Vision and Pattern Recognition, 2021, 12863-12872.

[48] Y. M. Jin, A. G. Khachaturyan, Atomic density function theory and modeling of microstructure evolution at the atomic scale, *Journal of Applied Physics*, 2006, **100**, 013519, doi: 10.1063/1.2213353.

[49] O. Adjaoud, K. Albe, Microstructure formation of metallic nanoglasses: insights from molecular dynamics simulations, *Acta Materialia*, 2018, **145**, 322-330, doi: 10.1016/J.ACTAMAT.2017.12.014.

[50] Y. Shibuta, K. Oguchi, T. Takaki, M. Ohno, Homogeneous nucleation and microstructure evolution in million-atom molecular dynamics simulation, *Scientific Reports*, 2015, **5**, 13534, doi: 10.1038/srep13534.

[51] L.-Q. Chen, Phase-field models for microstructure evolution,

Annual Review of Materials Research, 2002, **32**, 113-140, doi: 10.1146/annurev.matsci.32.112001.132041.

[52] N. Moelans, B. Blanpain, P. Wollants, An introduction to phase-field modeling of microstructure evolution, *Calphad*, 2008, **32**, 268-294, doi: 10.1016/j.calphad.2007.11.003.

[53] T. Rodgers, J. Madison, V. Tikare, Simulation of metal additive manufacturing microstructures using kinetic Monte Carlo, *Computational Materials Science*, 2017, **135**, 78-89, doi: 10.1016/j.commatsci.2017.03.053.

[54] E. A. Holm, C. C. Battaile, The computer simulation of microstructural evolution, *JOM*, 2001, **53**, 20-23, doi: 10.1007/s11837-001-0063-2.